lubricants

MDPI

Article

Numerical Simulation of Temperature Field, Velocity Field and Solidification Microstructure Evolution of Laser Cladding AlCoCrFeNi High Entropy Alloy Coatings

Andi Huang [1], Yilong Liu [2], Xin Li [3], Jingang Liu [1] and Shiping Yang [1,*]

[1] School of Mechanical Engineering and Mechanics, Xiangtan University, Xiangtan 411105, China; andy_h_china@foxmail.com (A.H.); jingangl2025@163.com (J.L.)
[2] School of Aeronautical Engineering, Hunan Automotive Engineering Vocational University, Zhuzhou 412001, China; liuyilong@stu.usc.edu.cn
[3] School of Mechanical Engineering, University of South China, Hengyang 421001, China; chigan688144@163.com
* Correspondence: shipingy2025@163.com

Abstract

In this study, a multiphysics coupling numerical model was developed to investigate the thermal-fluid dynamics and microstructure evolution during the laser metal deposition of AlCoCrFeNi high-entropy alloy (HEA) coatings on 430 stainless steel substrates. The model integrated laser-powder interactions, temperature-dependent material properties, and the coupled effects of buoyancy and Marangoni convection on melt pool dynamics. The simulation results were compared with experimental data to validate the model's effectiveness. The simulations revealed a strong bidirectional coupling between temperature and flow fields in the molten pool: the temperature distribution governed surface tension gradients that drove Marangoni convection patterns, while the resulting fluid motion dominated heat redistribution and pool morphology. Initially, the Peclet number (Pe_T) remained below 5, indicating conduction-controlled heat transfer with a hemispherical melt pool. As the process progressed, Pe_T exceeded 50 at maximum flow velocities of 2.31 mm/s, transitioning the pool from a circular to an elliptical geometry with peak temperatures reaching 2850 K, where Marangoni convection became the primary heat transfer mechanism. Solidification parameter distributions (G and R) were computed and quantitatively correlated with scanning electron microscopy (SEM)-observed microstructures to elucidate the columnar-to-equiaxed transition (CET). X-ray diffraction (XRD) analysis identified body-centered cubic (BCC), face-centered cubic (FCC), and ordered B2 phases within the coating. The resulting hierarchical microstructure, transitioning from fine equiaxed surface grains to coarse columnar interfacial grains, synergistically enhanced surface properties and established robust metallurgical bonding with the substrate.

Keywords: laser metal deposition; high-entropy alloy; multiphysics modeling; solidification microstructure

check for updates

Received: 17 November 2025
Revised: 8 December 2025
Accepted: 11 December 2025
Published: 12 December 2025

Citation: Huang, A.; Liu, Y.; Li, X.; Liu, J.; Yang, S. Numerical Simulation of Temperature Field, Velocity Field and Solidification Microstructure Evolution of Laser Cladding AlCoCrFeNi High Entropy Alloy Coatings. *Lubricants* **2025**, *13*, 541. https://doi.org/10.3390/lubricants13120541

Copyright: © 2025 by the authors. Licensee MDPI, Basel, Switzerland. This article is an open access article distributed under the terms and conditions of the Creative Commons Attribution (CC BY) license (https://creativecommons.org/licenses/by/4.0/).

1. Introduction

High-entropy alloy (HEA) have emerged as a novel class of materials that challenge the traditional alloy design paradigm by incorporating multiple principal elements in near-equiatomic ratios, typically forming simple solid solution phases such as face-centered cubic (FCC), body-centered cubic (BCC), or hexagonal close-packed (HCP) structures [1–3].

Since the pioneering work by Yeh et al. [4] and Cantor et al. [5], HEAs have attracted tremendous research interest due to their exceptional properties, including outstanding mechanical strength, superior corrosion resistance, excellent wear resistance, and remarkable thermal stability at elevated temperatures [6–8]. Among various HEA systems, AlCoCrFeNi alloys have been extensively investigated by researchers such as Zhang et al. [9] and Wang et al. [10], who demonstrated their unique combination of high hardness (>500 HV), good oxidation resistance up to 1000 °C, and tunable phase composition through aluminum content adjustment. A single-phase FCC solid solution is observed exclusively when the aluminum molar ratio remains below 0.45. As the Al content increases to the intermediate range of 0.45–0.88, a dual-phase region composed of both FCC and BCC solid solutions emerges. Ultimately, exceeding this threshold leads to a full structural transition into a single-phase BCC solid solution [11]. However, beyond chemical composition, the specific fabrication process also plays a decisive role in the phase transformation behavior of the alloy. For instance, A. Faraji et al. [12] synthesized AlCoCrFeNi HEAs using Spark Plasma Sintering (SPS). Their as-sintered microstructure consisted primarily of a dual-phase structure, but subsequent heat treatment at 1000 °C induced a significant transformation of the BCC phase into the FCC phase. In contrast, Shuai Li et al. [13]. fabricated AlCoCrFeNi coatings via laser cladding and observed that, regardless of variations in laser power, the coatings consistently retained a typical structure composed of A2 (disordered BCC) and B2 (ordered BCC) phases, with no significant precipitation of the FCC phase.

Laser metal deposition (LMD), also referred to as laser cladding, is an advanced additive manufacturing and surface modification technique that employs a high-energy laser beam to melt metallic powders, depositing them layer by layer onto substrates [14,15]. In comparison to conventional coating technologies, LMD presents several distinct advantages, including precise dimensional control, minimal thermal distortion, robust metallurgical bonding, and the ability to fabricate functionally graded materials [16–18]. Dobrzanski et al. [19] and Li et al. [20] have successfully utilized LMD to deposit high-entropy alloy (HEA) coatings for surface strengthening, demonstrating significant enhancements in wear resistance and corrosion protection. Nevertheless, the LMD process encompasses intricate multi-physical phenomena, such as rapid heating and cooling, dynamic melt pool flow, and non-equilibrium solidification, which collectively influence the final coating quality and microstructural characteristics [21,22].

Understanding the thermal–fluid coupling behavior and solidification dynamics during laser cladding is crucial for optimizing the process and controlling microstructure. Xiao et al. [23] utilized high-speed imaging to experimentally characterize complex Marangoni convection patterns in the melt pool, while Gan et al. [24] employed infrared thermography to measure temperature distributions during laser cladding. Nevertheless, experimental methods often face limitations due to high costs and challenges in capturing transient phenomena that occur at millisecond timescales. Consequently, numerical simulation has emerged as an indispensable complementary tool for a detailed investigation of process dynamics [25–27].

Significant progress has been achieved in the computational modeling of laser cladding processes. Early thermal models developed by Picasso et al. [28] and Qi et al. [29] primarily focused on pure heat conduction, neglecting the effects of melt pool convection. Subsequently, Ma et al. [30] and Li et al. [31] advanced this field by developing coupled thermal-fluid models that incorporate Marangoni convection, demonstrating that surface tension-driven flow has a substantial impact on melt pool morphology and temperature uniformity. In the realm of microstructure simulation, Körner et al. [32] were pioneers in integrating cellular automaton methods with finite element thermal analysis to predict dendritic growth during selective laser melting. More recently, Ma et al. [33] established

a multi-scale model that couples computational fluid dynamics (CFD) with phase-field methods to simulate grain structure evolution in the laser cladding of Inconel 718. For high-entropy alloy (HEA) systems specifically, Chen et al. [34] conducted a numerical investigation of the temperature field during the laser cladding of CoCrFeNi coatings, while Tian et al. [35] examined the influence of laser parameters on dilution rate through finite element analysis. However, comprehensive multiphysics modeling that simultaneously captures thermal-fluid coupling, solidification parameters (G, R), and microstructure evolution (columnar-to-equiaxed transition) remains limited, particularly for the AlCoCrFeNi/430SS dissimilar material system.

The present study aims to establish a comprehensive multiphysics coupling model for the laser metal deposition of AlCoCrFeNi HEAcoatings on 430 stainless steel substrates. This model integrates thermal analysis, fluid dynamics influenced by Marangoni convection, and predictions of solidification microstructure based on G-R relationships. Single-track experiments are conducted to validate the model's predictions, while the coating phase composition and microstructure are characterized using X-ray diffraction (XRD) and scanning electron microscopy (SEM). This work provides a fundamental understanding of the complex thermal-fluid-solidification coupling phenomena during the laser cladding of high-entropy alloy (HEA) and offers theoretical guidance for optimizing process parameters to achieve tailored microstructures and enhanced coating performance.

2. Materials and Methods

2.1. Materials Properties

An equiatomic mixture of Al, Co, Cr, Fe, and Ni powders (20 at.% each) was prepared as the cladding feedstock; their specific compositions are detailed in Table 1. Mechanical mixing was conducted using a YXQM-4L planetary ball mill (Miqi MITR Instrument Co., Ltd., Changsha, China) to achieve homogeneity. The milling process operated at 350 rpm for 5 h, employing 5 mm stainless steel grinding balls with a ball-to-powder weight ratio of 3:1. To eliminate adsorbed moisture prior to deposition, the blended powders were vacuum-dried at 60 °C for 3 h. Figure 1 illustrates the SEM morphologies of the powders before and after mixing. The substrates were machined from 10 mm thick 430 stainless steel plates into dimensions of 100 mm × 20 mm, with the substrate composition listed in Table 2.

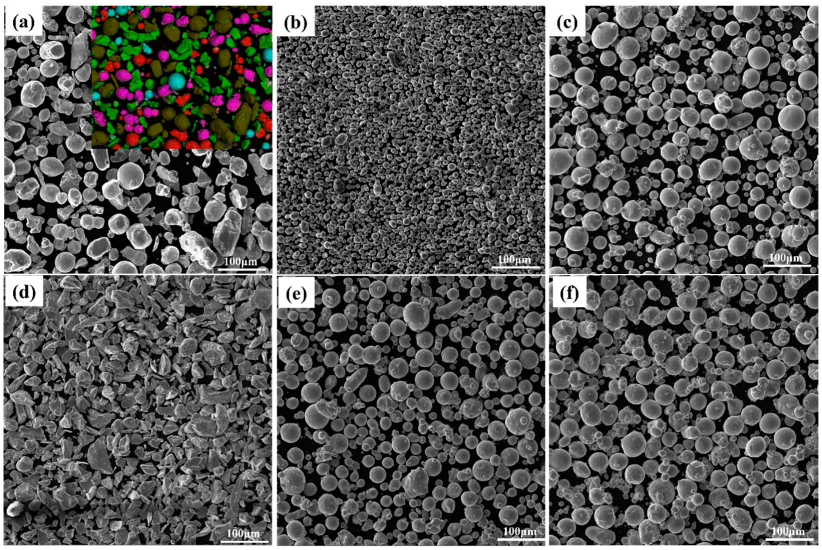


Figure 1. SEM image of mixed AlCoCrFeNi powder and five original powders: (**a**) AlCoCrFeNi and EDS spectrum, (**b**) Al powder, (**c**) Co powder, (**d**) Cr powder, (**e**) Fe powder, (**f**) Ni powder.

Table 1. Details of powders used for deposition.

S. No.	Element	Purity	Particle Size
1	Al	99.9%	45–106 µm
2	Co	99.9%	45–106 µm
3	Cr	99.9%	15–53 µm
4	Fe	99.9%	45–106 µm
5	Ni	99.9%	15–53 µm

Table 2. Chemical Composition of 430 Stainless Steel (wt.%).

C	Si	Mn	Ni	Cr	Fe
≤0.12	≤0.75	≤1	≤0.6	16~18	Bal.

The thermal properties utilized in this study were calculated using JMatPro software (V13 version), based on the elemental composition of the materials, as illustrated in Figure 2. During the Laser Metal Deposition (LMD) process, the abrupt changes in material properties are significant and warrant careful consideration. Consequently, the model incorporates additional thermal property parameters for both the substrate and the powder, as detailed in Table 3. Importantly, due to the interaction between the substrate material and the added powder within the melt pool, the thermal properties of the liquid metal are assumed to be a weighted average of the properties of the substrate and the powder. This relationship can be expressed as:

$$\alpha = \beta\alpha_{base} + (1 - \beta)\alpha_{pow} \quad (1)$$

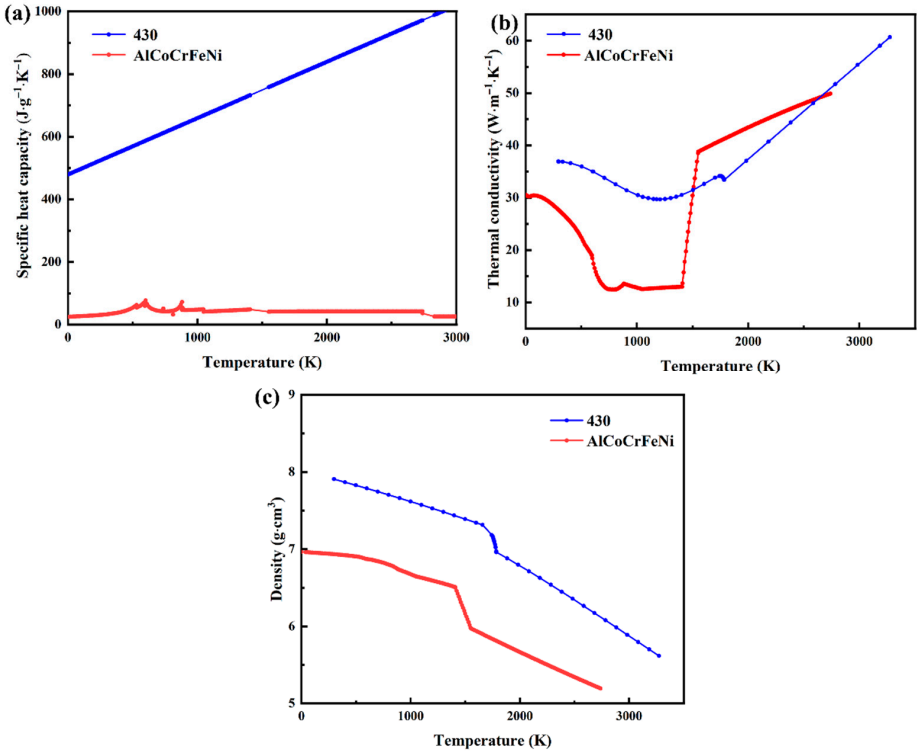


Figure 2. 430 stainless steel and AlCoCrFeNi thermophysical parameters: (**a**) Specific heat capacity; (**b**) Thermal conductivity; (**c**) Density.

Table 3. Performance of 430 stainless steel substrate and AlCoCrFeNi cladding material.

Parameter	430 Substrate	Cladding Layer (AlCoCrFeNi)
Solidus temperature, T_s (K)	1658.2	1683.2
Liquidus temperature, T_l (K)	1784.2	1824.7
Latent heat, L (J/g)	232	22.1
Melting temperature, T_m (K)	1721.2	1753.2
Solid phase-specific heat capacity, C_{p1} (J/kg/K)	500	565
Liquid phase-specific heat capacity, C_{p2} (J/kg/K)	850	1100

Here, α, α_{base}, and α_{pow} represent the thermophysical properties of the liquid metal, the substrate material (430 stainless steel), and the cladding material (AlCoCrFeNi), respectively. β denotes the mass fraction of the powder in the melt mixture. In this formulation, α may refer to parameters such as density, specific heat capacity, thermal conductivity, or surface tension. This approach effectively captures the combined thermal characteristics of the interacting constituents in the melt pool, providing a solid physical basis for subsequent simulations of heat transfer and fluid flow.

2.2. Laser Cladding Test and Characterization

Figure 3a illustrates the integrated laser deposition setup (Wuhan Ruike Fiber Laser Technology Co., Ltd., Wuhan, China) employed in this study. The apparatus features a fiber laser source (Model: RFL-C2000X) with a 75 μm core diameter, coupled with a programmable 3-axis CNC motion stage. Powder delivery was managed by an HW-05SF feeder unit using Argon as the carrier/shielding gas. Additionally, Figure 3b illustrates the schematic of the LMD process. Prior to the cladding, the 430 stainless steel substrate was polished to remove surface oxides, thereby enhancing the substrate's ability to absorb the laser energy [36]. The substrate was then cleaned with ethanol to eliminate any remaining impurities. Subsequently, AlCoCrFeNi powder particles were delivered into the melt pool via high-purity argon gas (used as both carrier and shielding gas), forming the HEA coating. It is important to note that the LMD parameters have a significant effect on the complex interactions between the laser beam and the melt pool. These parameters directly influence the flow dynamics, morphology, solidification behavior, and the quality of the coating formed. Following preliminary experimental validation, the optimized parameters listed in Table 4 were adopted, resulting in a high-quality coating. Therefore, the model in this study employs the same LMD parameter set to ensure the reliability of the results.

Table 4. Process parameters for laser cladding experiments and data used for calculations.

Process Parameters	Value
Laser power, p (W)	1450
Powder feeding rate, m_f (g/s)	0.9
Carrier gas flow rate, v_c (L/min)	7.5
Beam radius, r_d (mm)	1.5
Laser energy density, Led (J/mm^2)	205.7
Scanning speed, v (mm/s)	8
Mass flow radius, r_p (mm)	1.6
Emissivity, ε	0.6
Ambient temperature, (K)	293.15

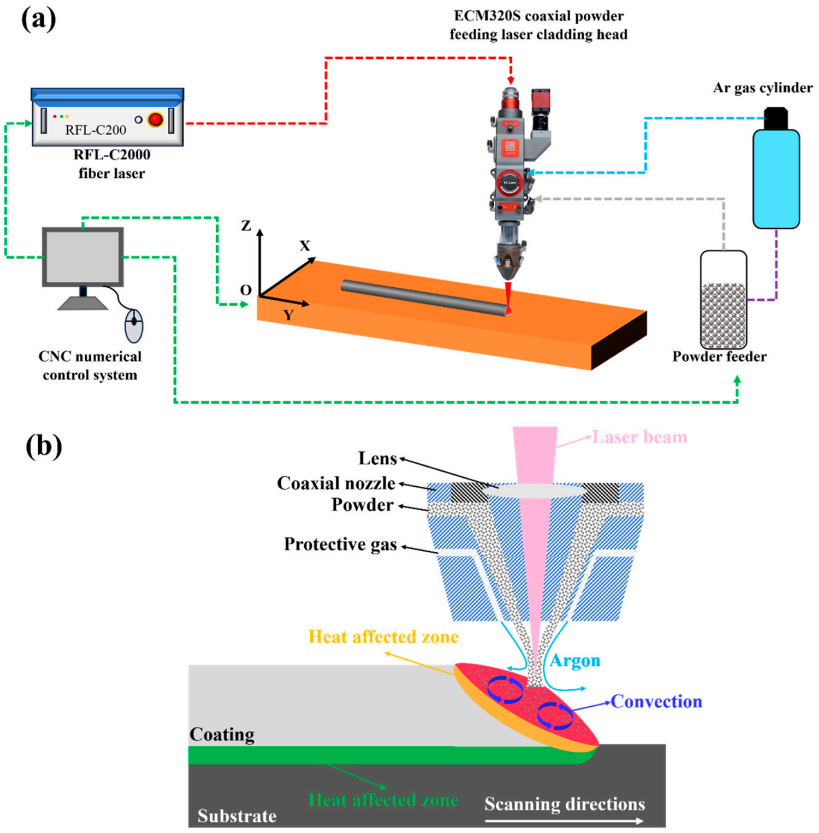


Figure 3. Laser metal deposition and characterization: (**a**) Experimental setup; (**b**) schematic diagram of LMD [37].

2.3. Sample Characterization Versus Performance Analysis

To facilitate microstructural examination, cross-sections were cut along the cladding centerline via wire-EDM. The samples underwent a meticulous grinding regime using 400–3000 mesh SiC papers of increasing fineness, followed by a 10 min ultrasonic decontamination step in an ethanol solution. The polished surfaces were then chemically etched for 15 s using a standard aqua regia solution ($HCl:HNO_3$ = 3:1). Ultimately, the resulting microstructures were characterized using a Scanning Electron Microscope (SEM) (Czech TESCAN model MIRA4, Brno-Kohoutovice, Czech Republic).

To facilitate XRD testing, the as-deposited AlCoCrFeNi alloy was machined into 10 mm^3 blocks using wire cutting. Phase structural analysis was subsequently carried out using a Panalytical Empyrean diffractometer (MiniFlex600, Japanese Neo-Confucianism, Tokyo, Japna) with Cu K radiation. The diffraction patterns were recorded under the conditions of 40 kV and 30 mA, scanning from 20° to 90° at a speed of 5°/min with a 0.02° step interval.

2.4. Simulation

The evolution of the melt pool in laser metal deposition (LMD) is a highly transient and dynamic process characterized by rapid and complex changes. Consequently, developing a comprehensive simulation model that accounts for all influencing factors is virtually impossible, as this would significantly increase computational costs and potentially result in an overly complex outcome. Therefore, to ensure the model's practicality and the effectiveness of the research, reasonable simplifying assumptions must be made. These assumptions are grounded in the accuracy of the research objectives and the necessity for realistic results, aiming to minimize computational resource consumption while maintaining the validity and applicability of the simulation outcomes. The simplified assumptions are as follows:

1. The laser heat input is assumed to follow a Gaussian distribution, and the heat is directly applied to the surface of the melt pool.
2. It is assumed that all powder particles entering the melt pool fully participate in the formation of the coating.
3. The heat flux for heating the powder and the heat loss due to evaporation are neglected.
4. The fluid flow in the melt pool is assumed to be incompressible, Newtonian, and laminar, with no consideration of the effects of the carrier gas or shielding gas on the melt pool.
5. The mushy zone, defined as the region where the temperature lies between the solidus and liquidus, is modeled as a porous medium with isotropic permeability.
6. It is assumed that there is no diffusion in the solid phase, meaning that the solidified material does not contribute to mass transfer by diffusion.
7. The concentration distribution of the powder is assumed to follow a Gaussian distribution, and any powder falling into the melt pool is immediately melted.
8. The attenuation of laser energy through the powder flow is neglected.

2.4.1. Governing Equations

Phase-Change Heat-Transfer

To accurately simulate the LMD process, the energy distribution of the laser beam and the movement of the heat source must be considered. A Gaussian distribution model is used to describe the power density distribution of the laser heat source (Equation (2)), which reflects the characteristic of higher energy at the center of the laser beam that gradually decreases outward. This distribution is crucial for the formation of the melt pool and the evolution of the temperature field. The initial power density distribution of laser beam was expressed as [38,39]:

$$E = \frac{2\mu p}{\pi r_d^2} \exp\left(-\frac{2[(x-vt)^2 + (y)^2]}{r_d^2}\right) \tag{2}$$

where μ, p, r_d, and v represent the absorption rate, laser power, laser spot radius, and scanning speed, respectively, while (x, y) denotes the spot center coordinates.

$$\rho C_p \frac{\partial T}{\partial t} + \rho C_p u \cdot \nabla T + \nabla \cdot q = E + h(T - T_0) + \varepsilon\sigma(T^4 - T^0) \tag{3}$$

$$q = -k\nabla T \tag{4}$$

$$\rho = \theta_1\rho_1 + \theta_2\rho_2 \tag{5}$$

$$k = \theta_1 k_1 + \theta_2 k_2 \tag{6}$$

$$\theta_1 + \theta_2 = 1 \tag{7}$$

the terms on the right-hand side of the equation represent heat accumulation, convective heat transfer, and thermal conduction, respectively. Here, ρ denotes the material density, C_p the specific heat capacity, T the temperature, u the velocity vector, k the thermal conductivity, h the convective heat transfer coefficient, T^0 the ambient temperature, ε the surface emissivity, and σ the Stefan–Boltzmann constant. In the pasty region, the mass fraction (β_z) is defined as:

$$\beta_z = \frac{1}{2}\frac{\theta_2\rho_2 - \theta_1\rho_1}{\theta_1\rho_1 + \theta_2\rho_2} \tag{8}$$

where θ_1 and θ_2 represent a solid portion and a liquid portion, respectively. ρ_1 and ρ_2 represent solid density and liquid density, respectively. Furthermore, the C_p used in the heat equation is given by,

$$C_p = \frac{1}{\rho}\left(\theta_1\rho_1 C_{p,1} + \theta_2\rho_2 C_{p,2}\right) + \iota_{1\to 2}\frac{\partial \beta_z}{\partial \tau} \tag{9}$$

where $C_{p,1}$ and $C_{p,2}$ are the specific heat capacities of the respective phases, and $l_{1\longrightarrow 2}$ corresponds to the enthalpy change across the solidus–liquidus interval.

Fluid Flow Model

Under the specified assumptions, the governing fluid flow equations were established by coupling the Navier–Stokes and continuity relations to ensure the simultaneous conservation of momentum and mass, As shown in the following Formulas (10)–(13) [40].

$$\rho\nabla \cdot u = 0 \tag{10}$$

$$\rho\frac{\partial u}{\partial t} + \rho(u \cdot \nabla)u = \nabla \cdot [-\rho I + K] + F + \rho g \tag{11}$$

$$K = \mu\left(\nabla u + (\nabla u)^T\right) \tag{12}$$

$$\left[-pI + \mu\left(\nabla u + (\nabla u)^T\right) - \frac{2}{3}\mu(\nabla \cdot u)I\right]n = \gamma\nabla_t T \tag{13}$$

In the equation, ρ denotes the material density, I the identity tensor, u the dynamic viscosity of the liquid metal, p the fluid pressure, T the temperature, F the volumetric force acting on the fluid, C_p the specific heat capacity, K the thermal conductivity, γ the surface tension, and $\nabla_t\, T$ the tangential temperature gradient.

2.4.2. Initial and Boundary Conditions

The heat flux boundary conditions at the gas–liquid surface are as follows:

$$-n \cdot q = e_1 + h(T - T_0) + \varepsilon\sigma(T^4 - T_0^4) \tag{14}$$

the right-hand side consists of three terms accounting for the effective laser heat input, convective heat loss, and radiative heat loss, respectively, with h denoting the modified convective heat transfer coefficient. The symmetric plane and the base are adiabatic boundaries:

$$-n \cdot q = 0 \tag{15}$$

The boundary conditions of the liquid–gas interface momentum equation are given by [41],

$$F_{L/G} = \lambda n^*\kappa - \nabla_s T\frac{d\lambda}{dT} \tag{16}$$

The two components on the right-hand side of Equation (16) correspond to the capillary force and the thermocapillary force, respectively. In this context, λ represents the surface tension, n^* is the normal vector to the surface, and k is the curvature of the surface.

The dynamic shape of the melt pool surface is explicitly modeled using a moving mesh approach based on the Arbitrary Lagrangian-Eulerian (ALE) method [42]. At the liquid/gas interface, two velocities are taken into account: the velocity of fluid flow and the velocity of boundary movement caused by mass addition [43]. These can be represented as follows:

$$V_{L/G} = u \cdot n^* + V_p \cdot n^* \tag{17}$$

Here, u represents the fluid flow velocity at the liquid/gas interface, while V_p denotes the boundary movement velocity due to mass addition. The calculation of V_p is given by the following equation:

$$V_p = \frac{2m_p 0.15}{\rho_i \pi r_p^2} \exp\left(\frac{-2\left((x - V_1 t)^2 + y^2\right)}{r_p^2}\right) Z \quad (18)$$

where m_p represents the mass flow rate, ρ_i represents the density of the powder, r_p represents the mass flow radius, and Z represents the unit vector in the z-direction.

To enhance computational efficiency, symmetric boundary conditions were applied, allowing for the calculation of only half of the model. The substrate dimensions are 6 mm × 2 mm × 1 mm. The model is discretized using tetrahedral elements, with local mesh refinement in critical regions to accurately capture the temperature history, as shown in Figure 4a. In the refined region, the minimum grid size is 9 μm, and the maximum is 210 μm. The temperature field distribution at t = 0.2 s is computed using the software's 3D imaging function, as depicted in Figure 4b.

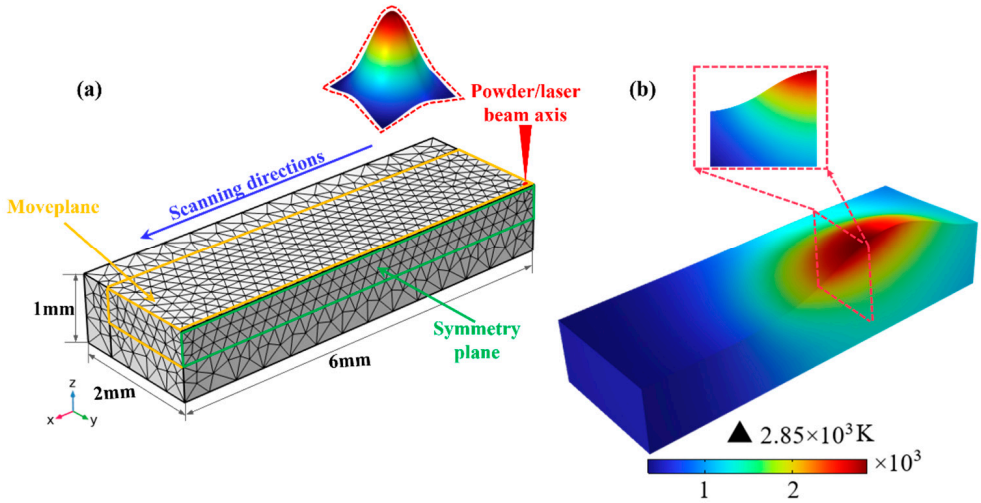


Figure 4. Model: (**a**) model boundary conditions; (**b**) calculation results at t = 0.2 s.

3. Results

3.1. Thermal History and Velocity Field

Figure 5a–d illustrates the calculated temperature field distribution at various time points, where the temperature is represented by contour lines. The red isotherm indicates the liquidus temperature, while the black isotherm denotes the solidus temperature. Initially, during the laser deposition process, the temperature at the center of the molten bath rises sharply due to the rapid heating from the laser heat flux. Once the temperature surpasses the solidus of the substrate, a solid–liquid phase transition occurs, leading to the formation of the molten bath. In Figure 5a, which corresponds to 0.05 s, the laser irradiation causes a marked increase in temperature in the central region of the molten bath, resulting in a distinct high-temperature zone. The molten bath exhibits a hemispheric morphology, primarily due to heat conduction within the bath, which dominates the temperature distribution. As time progresses, Figure 5b and 5c depict the gradual outward expansion of the temperature fields at 0.2 s and 0.3 s, respectively. During this period, the liquid metal begins to flow, and the Marangoni convection effect becomes increasingly significant as the temperature gradient changes. Heat diffuses from the high-temperature region to the low-temperature region, causing the bath morphology to become wider and shallower,

while the temperature distribution approaches uniformity. Finally, at 0.4 s, as shown in Figure 5d, the temperature of the molten bath stabilizes. Heat transfer is predominantly governed by convection, and the temperature field within the molten bath reaches dynamic equilibrium, further indicating the synergistic effect between thermal convection and heat conduction, leading to a uniform temperature distribution within the molten bath.

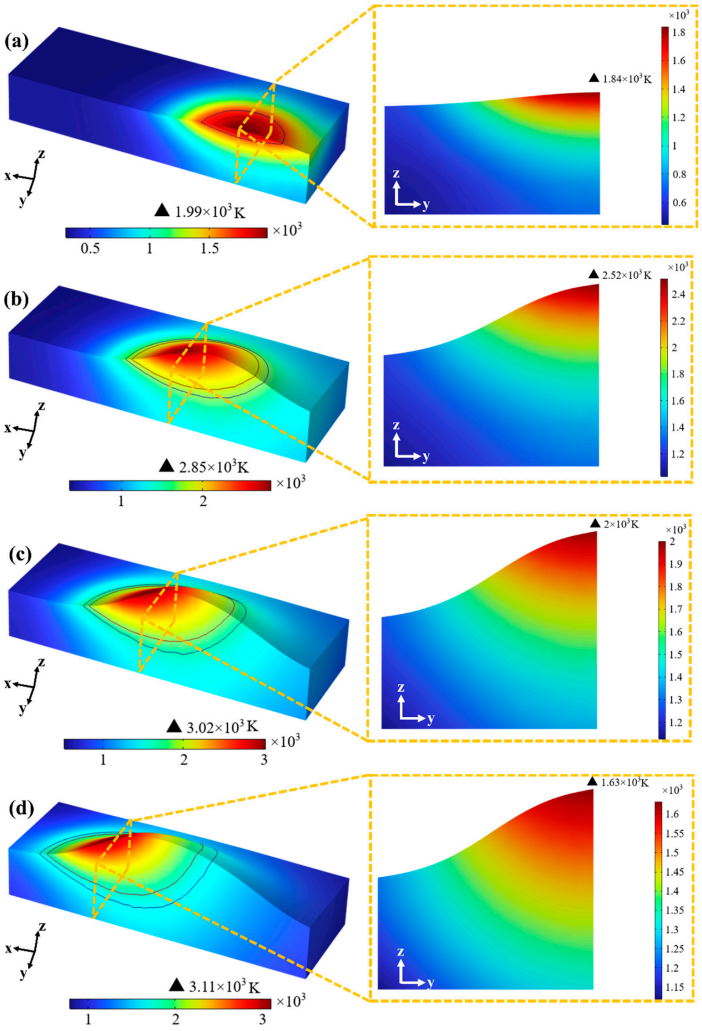


Figure 5. Simulated temperature field of molten bath at different times: (**a**) 0.05 s; (**b**) 0.2; (**c**) 0.3; (**d**) 0.4.

In addition, liquid metal flow in a molten bath has an effect on heat transfer, and the importance of convection to heat transfer can be assessed by the Peclet number,

$$Pe_T = \frac{uL_R}{\alpha_h} \tag{19}$$

In the formula, u is the characteristic liquid velocity in the bath, L_R is the characteristic length of the bath radius, and α_h is the material thermal diffusivity. This "Peclet number" can be calculated to determine whether heat conduction or thermal convection plays a dominant role in the molten pool [44]. Figure 6 displays the simulated velocity fields at t = 0.1 s and t = 0.3 s, with arrows indicating the direction of flow. The liquid metal flows from the center of the molten pool towards its outer edges. Additionally, the flow velocity is lowest in the region with the highest temperature. Considering that the surface tension of the liquid is negatively correlated with temperature [45,46], the temperature increases as one moves closer to the center of the molten pool. As a result, the liquid metal flows

from areas of lower surface tension to areas of higher surface tension. At t = 0.1 s, as shown in Figure 6a, the maximum flow velocity of the molten metal is 0.1 mm/s, resulting in a Peclet number (Pe_T, Equation (19)) less than 5. In this case, heat conduction plays a dominant role in heat transfer, leading to the formation of a nearly hemispherical molten pool boundary. As convection strengthens and the flow velocity increases, the molten pool undergoes further development, transforming from a circular shape to an elliptical one, as seen in Figure 6b. At this stage, the maximum flow velocity reaches 2.31 mm/s, and the Peclet number in the molten pool exceeds 50, indicating that heat transfer is now primarily governed by convection. The negative temperature coefficient of surface tension causes the liquid metal to flow outward from the center of the pool, enhancing heat transfer within the molten pool. Consequently, the temperature gradient becomes much lower than in cases where fluid flow is neglected. The increased outward flow results in a wider and shallower molten pool boundary.

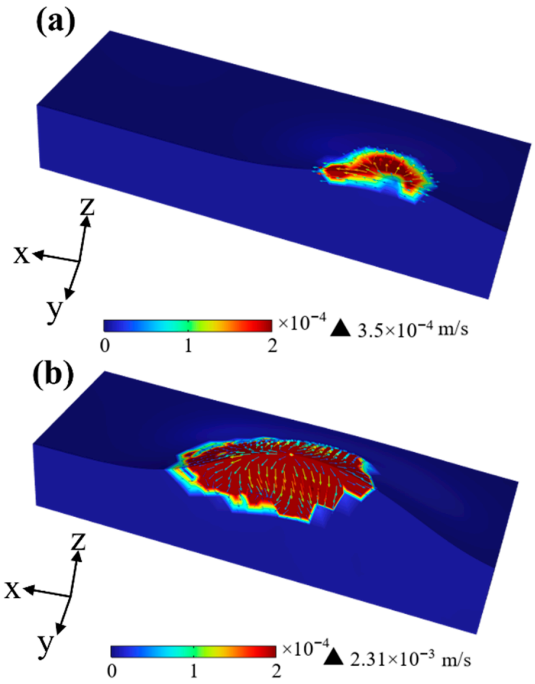


Figure 6. Molten pools at different times simulate velocity fields: (**a**) 0.1 s; (**b**) 0.3 s.

Based on the superposition analysis of the temperature and velocity fields presented in Figure 7, at the X = 0.8 mm section, the molten pool exhibits characteristics typical of Marangoni convection dominance. The longitudinal section (a) reveals that the temperature distribution of the molten pool resembles a 'mushroom shape,' with the peak temperature at the center reaching 2850 K. The velocity vector indicates that the liquid metal flows from the high-temperature center towards the low-temperature edge, forming a backflow vortex at the bottom. The top view (b) illustrates a concentric temperature distribution alongside a radially divergent velocity field. The shape of the molten pool transitions from an initial hemispherical form to an elliptical configuration, achieving a maximum flow velocity of 2.31 mm/s. At this juncture, the Peckley number surpasses 50, signifying that convective heat transfer has supplanted heat conduction as the predominant mechanism. This vigorous Marangoni convection not only facilitates the lateral expansion of the molten pool, resulting in a 'dish-shaped' morphology, but also enhances the thorough mixing of alloying elements and the effective escape of gases. These factors collectively create favorable conditions for achieving a high-quality AlCoCrFeNi coating characterized by uniform composition and the absence of porosity defects. The simulation results exhibit a

high degree of agreement with the experimentally observed cross-sectional morphology of the coating.

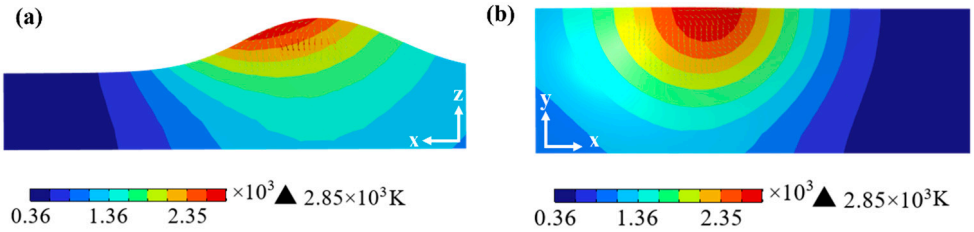


Figure 7. The superimposed temperature field and velocity field of the X = 0.8 mm molten bath: (**a**) Measure view; (**b**) overhead view.

3.2. Verification of Model

To validate the accuracy of the multiphysics coupling model, Figure 8a presents a cross-sectional schematic of the single-track coating. A comparative analysis of experimental and numerical simulation results highlights several key geometric parameters, including coating height (h), coating depth (H), melt pool width (W), and coating dilution rate (η). These parameters play a crucial role in the coating process, directly influencing the model's precision and reliability. By examining these factors, the study not only verifies the effectiveness of the multiphysics model but also provides insights into how these parameters interact and affect coating quality. This approach enables further refinement and optimization of the model, ensuring more accurate predictions of coating behavior in practical applications. The dilution ratio (η) is calculated as follows:

$$\eta = \frac{h}{H + h} \times 100\% \tag{20}$$

where H represents the coating height (μm), and h represents the bath depth (μm).

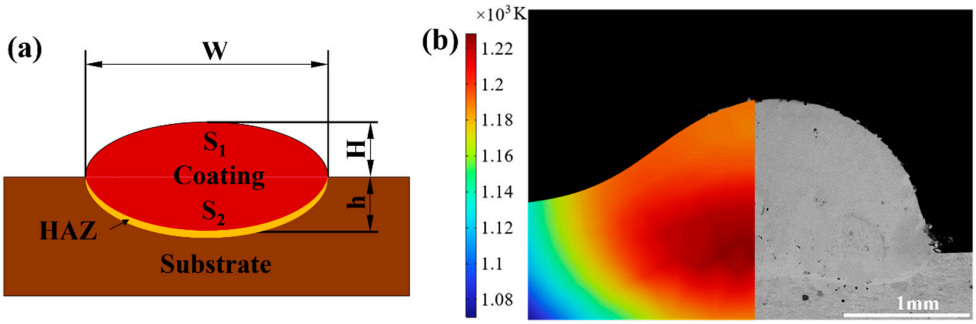


Figure 8. Cross-sectional schematic: (**a**) geometric features (**b**) simulated and actual molten pools.

Figure 8b presents the experimental and simulated cross-sectional profiles of the AlCoCrFeNi single-track coating. The experimental results show that the coating is free of pores and cracks, exhibiting excellent formation quality. This can be attributed to the high heat input during the Laser Metal Deposition (LMD) process, which maintains the melt pool temperature at elevated levels for an extended period. As a result, the gases had sufficient time to escape from the melt pool, preventing the formation of pores and ensuring a high-quality coating.

From the perspective of numerical simulation, the established model demonstrates a strong ability to predict the coating's geometric shape. The simulated cross-sectional shape closely matches the experimental observations. Specifically, the simulated melt pool topography forms a typical dish-shaped arc, and the coating exhibits a lateral expansion due to Marangoni convection, consistent with previous simulation predictions.

As shown in Table 5, a comparison of the key geometric parameters from both experimental and simulated results reveals some discrepancies. The experimental values for coating width (W), height (H), and melt pool depth (h) were measured as 2931.05 μm, 1199.6 μm, and 340.8 μm, respectively. The corresponding simulated values were 3075.8 μm, 991.5 μm, and 400.7 μm. The dilution rate (η) calculated using formula (20) was 22.5% for the experiment and 28.7% for the simulation. The errors between experimental and simulated results for W, H, h, η were 4.94%, 17.35%, 17.36%, and 27.60%, respectively. While the overall discrepancy between the experimental and simulated results is not large, the simulation slightly overestimates W, H, η compared to the experimental measurements. These deviations can be attributed to several factors. Firstly, the model does not account for the coating's evaporation phenomenon. The simulated melt pool temperature exceeds the powder's boiling point, leading to the evaporation of some powder, which reduces the actual coating volume. This phenomenon is not included in the simulation, resulting in slightly larger coating width and depth in the simulated results compared to the experimental values. Secondly, the model neglects the influence of shielding gas. In the actual LMD process, the pressure of the shielding gas affects the velocity field of the free surface, which in turn promotes the flow of liquid into the melt pool. This accelerates the coating growth rate, but this effect is not considered in the simulation, leading to a simulated coating height (H) that is slightly larger than the experimental measurement. Lastly, the model fails to consider the impact of the coating's growth on the laser incidence angle. In practice, as the coating grows, the laser incidence angle changes, which affects the laser absorption efficiency and, consequently, the heat input. Since the laser used in the experiment is polarized, the change in the incidence angle due to coating growth reduces the laser's absorption rate. As a result, the heat input during the actual process is lower, leading to weaker thermal penetration along the coating height direction. This contributes to the slightly higher coating height and depth in the simulated results compared to the experimental data.

Table 5. Comparison of geometric parameters of experimental and simulation results.

	W (μm)	H (μm)	h (μm)	η (%)
Experiment	2931.05	1199.69	340.82	22.55
Simulation	3075.83	991.53	400.73	28.78
Error (%)	4.94	17.35	17.36	27.60

By integrating XRD pattern analysis with molten pool temperature field simulation, a comprehensive understanding of the phase transformation behavior and temperature distribution during laser deposition of AlCoCrFeNi alloy can be achieved. As shown in Figure 9, the XRD pattern reveals that the alloy is primarily composed of BCC, FCC, and ordered B2 phases. Based on semi-quantitative analysis using the RIR method, as presented in Table 6, the coating consists of BCC disordered phase (49.8 wt.%, 50.7 vol.%), FCC phase (29.5 wt.%, 27.7 vol.%), and B2 ordered phase (20.7 wt.%, 21.6 vol.%), with a phase fraction ratio of approximately 5:3:2. The FCC phase tends to form at higher temperatures, while the BCC phase remains stable at lower cooling rates. The formation of the ordered B2 phase is influenced by both alloy composition and temperature field evolution, typically appearing gradually during the cooling stage. According to the molten pool temperature field simulation shown in Figure 5, temperature variations induced by laser heating can be clearly observed. At approximately 0.4 s, the temperature stabilizes, with heat transfer dominated by convection, indicating that the temperature field reaches dynamic equilibrium. During this process, FCC phase formation is primarily controlled by laser heat input, while the BCC phase stabilizes progressively during cooling, with the

ordered B2 phase forming at this stage. The BCC phase accounts for a volume fraction of 50.7 vol.%, serving as the dominant phase, while the FCC phase has a volume fraction of 27.7 vol.%, which is attributed to the instantaneous increase in laser energy during the laser deposition process, causing a momentary rise in molten pool temperature and partial transformation from BCC to FCC. The B2 ordered phase has a volume fraction of 21.6 vol.%, indicating significant ordering under rapid cooling conditions. The combined analysis of temperature field simulation and XRD results provides deeper insights into the formation mechanisms and spatial distribution of different phases, revealing the dominant roles of FCC and BCC structures in the alloy while confirming the presence of the ordered B2 phase at a smaller volume fraction. The dynamic interplay between temperature field evolution and phase transformations significantly influences the microstructure and properties of AlCoCrFeNi alloy, providing valuable guidance for optimizing laser deposition processes to enhance mechanical performance and thermal stability.

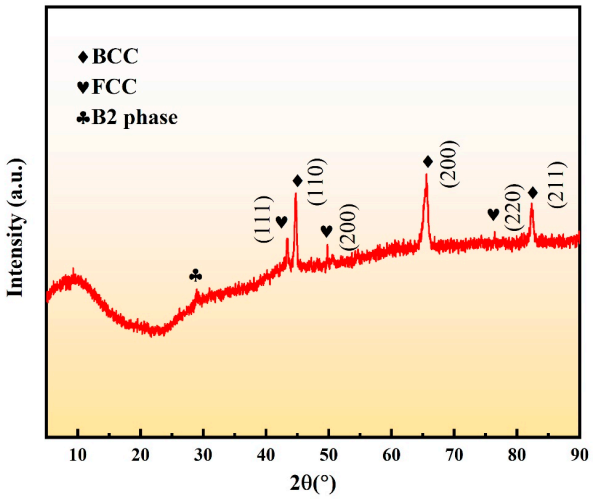


Figure 9. XRD results for coated surfaces.

Table 6. RIR method three-phase quantitative calculation data.

Crystalline Phase	Strongest Peak Crystal Plane	2θ (°)	Peak Intensity	RIR	Mass Fraction (wt.%)	Volume Fraction (vol.%)
FCC	(111)	43.40	3613.48	2.0	29.8	27.7
BCC	(200)	65.56	5486.14	1.8	49.8	50.7
B2	(100)	28.98	2409.47	1.9	20.7	21.6

Semi-quantitative phase analysis was performed based on the integrated intensity of the strongest diffraction peak of each phase using the intensity ratio (RIR) method. The calculation is as follows:

$$W_\alpha = \frac{I_\alpha / RI_\alpha}{\sum_i (I_i / RI_i)} \times 100\% \quad (21)$$

$$V_\alpha = \frac{W_\alpha / p_\alpha}{\sum_i (W_i / p_i)} \times 100\% \quad (22)$$

Figure 10 presents the EDS line scan results across the AlCoCrFeNi coating cross-section, revealing the elemental distribution from the coating surface to the substrate interface. The line scan profile demonstrates that the principal elements of the coating, Fe, Cr, Co, Ni, and Al, are relatively uniformly distributed throughout the coating thickness

of 1250 μm. This compositional homogeneity indicates that Marangoni convection-driven flow in the molten pool during the laser deposition process promotes effective elemental diffusion between the powder feedstock and substrate, thereby establishing strong metallurgical bonding at the coating-substrate interface. A distinct compositional transition occurs at approximately 1250 μm from the scan origin, indicating that the coating thickness is approximately 1250 μm. The oxygen content in the coating is 2.14 wt.%, demonstrating that the shielding gas provides excellent protection during the laser cladding process, minimizing oxidation of the coating to the greatest extent and preserving the coating quality.

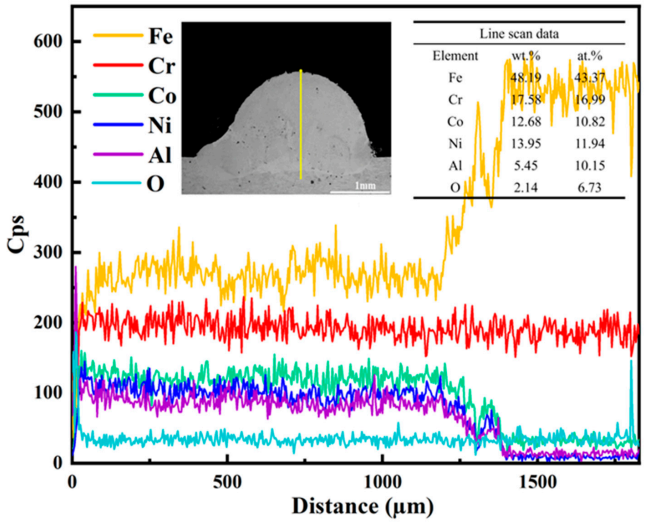


Figure 10. Coating section line sweep EDS results.

3.3. Pool Solidification Behavior

The evolution of the coating's solidification microstructure is primarily influenced by local solidification conditions, including the temperature gradient (G) and solidification rate (R) at the liquid/solid interface of the molten pool. The temperature gradient reflects the rate of heat transfer between the liquid and solid phases, while the solidification rate determines the speed at which the phase transition from liquid to solid occurs. Together, these two factors directly impact the coating's microstructure, such as grain size, porosity, and crystallization pattern. Therefore, to accurately understand and control the final quality and performance of the coating, it is essential to thoroughly analyze the temperature field distribution during the solidification process. This analysis helps optimize the solidification process and improve the coating's structural characteristics. G at the solidification interface can be calculated as follows:

$$G_i = \frac{\partial T}{\partial d} \tag{23}$$

$$G = \sqrt{G_x^2 + G_y^2 + G_z^2} \tag{24}$$

Here, i denotes the orientation of the temperature gradient, while G_x, G_y, and G_z correspond to its spatial components along the X, Y, and Z axes, respectively. The solidification rate (R) is subsequently determined using the following equation:

$$R_c = \frac{\partial T}{\partial t} \tag{25}$$

$$R = \frac{1}{G} \times \frac{\partial T}{\partial t} \tag{26}$$

The G-value distribution illustrates the variation in the temperature gradient at the liquid/solid interface, with elevated G-values indicating regions of rapid cooling and finer

microstructures. As depicted in the cross-sectional G-value distribution in Figure 11a, the maximum G-value, as defined by Equations (23) and (24), is prominently observed in the lower region of the coating, adjacent to the unmelted substrate, with a value of 1.8×10^5 K/m. This observation signifies a higher temperature gradient in the lower region, which results in accelerated cooling. The R-value distribution, represented by Equations (25) and (26), delineates the solidification rate, which governs the speed at which the material transitions from liquid to solid. A higher solidification rate yields smaller grains and diminished porosity, whereas a lower solidification rate may lead to coarser grains and potential defects. The R-value distribution, derived from the simulation, is illustrated in Figure 11b. Notably, the R-value peaks at the top of the coating (0.018×10^{-2} m/s), while it diminishes at the bottom, indicating that solidification occurs more rapidly at the top.

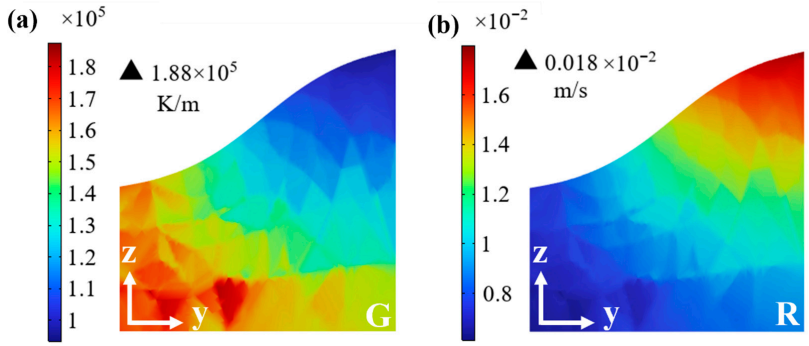


Figure 11. Simulation results of G and R: (**a**) G-value distribution (**b**) R-value distribution.

In Figure 12a, G*R represents the cooling rate, which follows a trend similar to that of the solidification rate. From the top to the bottom of the coating, the cooling rate decreases, with the highest cooling rate at the top and the lowest at the bottom. As the cooling rate decreases, the suppression of grain growth weakens, leading to an increase in grain size from top to bottom. In Figure 12b, G/R represents the shape control factor, which governs the morphological changes of the microstructure within the coating. The G/R values in the molten pool range from 3.22×10^6 s·K·m^{-2} to 3.02×10^7 s·K·m^{-2}. The G/R value is smaller at the top and larger at the bottom. As shown in Figure 13, higher G/R values promote the formation of planar grains, while lower G/R values favor the formation of equiaxed grains.

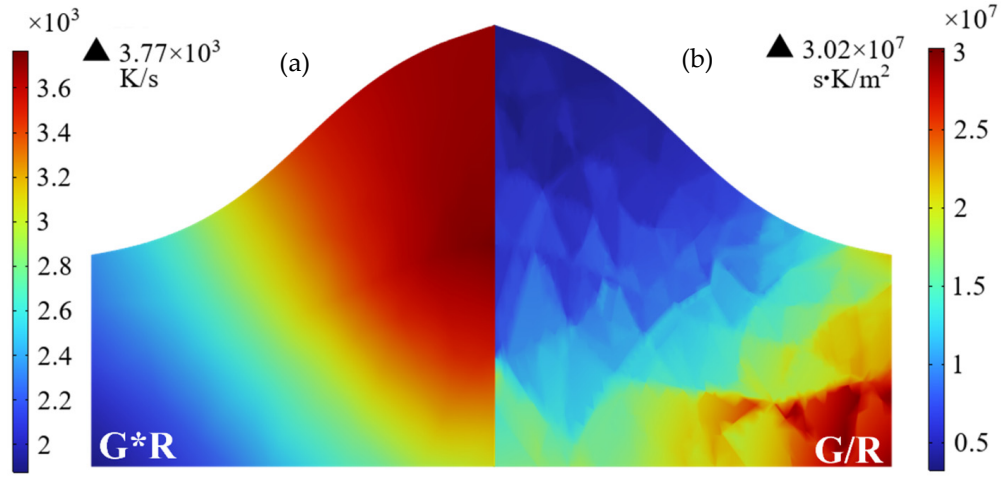


Figure 12. The simulated cooling rate G*R (**a**) and the shape control factor G/R value (**b**) distribution.

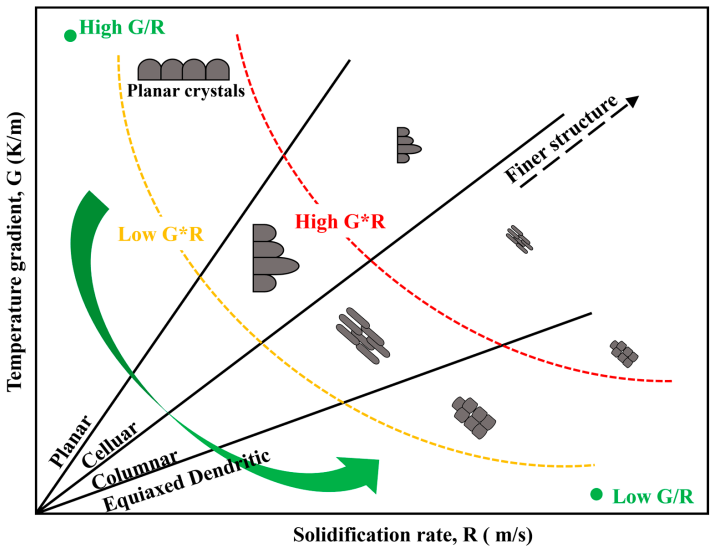


Figure 13. The effects of G and R on the shape and size of solidified tissue.

Figure 13 presents a solidification microstructure selection map illustrating the coupled effects of temperature gradient (G) and solidification rate (R) on grain morphology and size. The map delineates four distinct solidification regimes: planar, cellular, columnar dendritic, and equiaxed dendritic structures, separated by critical G/R and G*R boundaries. The green arrow trajectory from high G/R (bottom of coating, 3.02×10^7 s·K·m^{-2}) to low G/R (top of coating, 3.22×10^6 s·K·m^{-2}) demonstrates the microstructural evolution along the coating depth: at the substrate interface where G reaches 1.8×10^5 K/m with low R, the elevated G/R ratio suppresses constitutional undercooling and promotes planar or columnar grain growth with preferential orientation; conversely, at the coating top where R increases to 0.018×10^{-2} m/s while G decreases, the reduced G/R ratio intensifies constitutional undercooling and facilitates the columnar-to-equiaxed transition (CET). The accompanying SEM images validate these predictions, revealing oriented columnar structures at high G/R regions and randomly distributed equiaxed grains at low G/R regions. Furthermore, the cooling rate (G*R) gradient from top to bottom results in grain coarsening along the build direction, as lower cooling rates allow extended growth time. This microstructural gradient-transitioning from fine equiaxed grains at the surface to coarse columnar grains at the interface-is advantageous for coating performance, providing isotropic wear resistance at the surface while ensuring strong metallurgical bonding with the substrate.

Figure 14 illustrates the microstructural characteristics across different regions of the coating cross-section, revealing that equiaxed crystals are predominantly distributed in the top region, while columnar crystals are mainly concentrated in the middle and bottom regions. As depicted in Figure 14a, the coating exhibits a dense and defect-free "dish-shaped" geometry, visually validating the reshaping effect of Marangoni convection on the melt pool morphology. Figure 14d displays the microstructure at the bottom of the coating, where the elevated G/R ratio suppresses constitutional undercooling, inducing the directional growth of coarse columnar crystals along the heat flow direction; this mechanism ensures robust metallurgical bonding with the substrate. In the middle region, as shown in Figure 14c, a transition characterized by grain refinement is observed. In contrast, at the top of the coating, as shown in Figure 14b, the sharp decrease in the G/R ratio significantly broadens the constitutional undercooling zone, ultimately facilitating the formation of fine equiaxed grain structures. The consistency between the experimentally observed microstructure and the simulation results indirectly verifies the validity and accuracy of the proposed model.

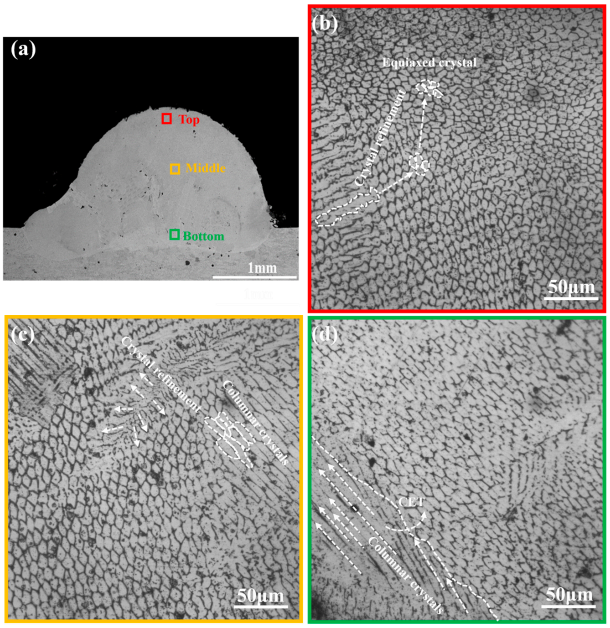


Figure 14. SEM images of different areas of the coating cross section: (**a**) Overall coating morphology (**b**) top of coating (**c**) middle of coating (**d**) bottom of coating.

4. Conclusions

The LMD process of AlCoCrFeNi high-entropy alloy (HEA) coatings on 430 stainless steel substrates was investigated via numerical simulation and single-track experimental validation. By integrating experimental observations with simulation results, the microstructure evolution of the coating was analyzed. The main conclusions are drawn as follows:

(1) The simulated geometric characteristics of the coating exhibit good agreement with experimental measurements, showing relative errors of 4.94% (W), 17.35% (H), and 17.36% (h), respectively, which verifies the reliability of the model. Furthermore, the simulation reveals a transition in melt pool dynamics from conduction-dominated ($Pe_t < 5$, hemispherical shape) to Marangoni convection-dominated ($Pe_t > 50$, elliptical shape). The peak temperature reaches 2850 K with a maximum flow velocity of 2.31 mm/s. The temperature and flow fields are strongly coupled, where Marangoni convection significantly promotes efficient mixing and degassing.

(2) Numerical simulations were performed to investigate the evolution of solidification parameters (G and R) during LMD. Results showed that the temperature gradient (G) peaked at 1.8×10^5 K/m at the bottom of the coating and decreased towards the top. Conversely, the solidification rate (R) exhibited an inverse trend, increasing to a maximum of 0.018 m/s at the surface. Consequently, the resulting cooling rate (G*R) profile led to grain coarsening along the build direction.

(3) The microstructure evolution was governed by the G/R ratio, creating a gradient from 3.22×10^6 to 3.02×10^7 s·K·m^{-2}. This variation caused the morphology to evolve from planar to cellular and finally equiaxed dendrites from the interface upwards. SEM analysis validated this trend and indicated that grain refinement was driven by increasing cooling rates (G*R). Crucially, the accumulation of constitutional undercooling ahead of the columnar interface promoted the nucleation of equiaxed grains, leading to a distinct CET behavior.

(4) XRD analysis revealed that the AlCoCrFeNi HEAs coating primarily consists of BCC, FCC, and ordered B2 phases, with FCC phase forming during rapid heating and BCC phase stabilizing during cooling. High-quality, defect-free coatings were successfully fabricated due to sufficient energy input maintaining elevated temperatures (>2800 K)

for effective gas escape. As a result, the functionally graded microstructure can achieve enhanced surface properties while ensuring strong substrate bonding.

Author Contributions: Conceptualization, A.H.; Methodology, A.H.; Software, X.L.; Validation, X.L.; Formal analysis, Y.L.; Investigation, Y.L. and J.L.; Data curation, Y.L.; Writing—original draft, A.H.; Writing—review & editing, S.Y.; Visualization, S.Y.; Supervision, J.L. and S.Y. All authors have read and agreed to the published version of the manuscript.

Funding: This work is supported by the Xiangtan University Graduate Research and Innovation Project Fund (XDCX2024Y231). The authors thank the other participants in the project for their cooperation.

Data Availability Statement: The original contributions presented in this study are included in the article. Further inquiries can be directed to the corresponding author.

Conflicts of Interest: The authors declare no conflict of interest.

References

1. Odetola, P.I.; Babalola, B.J.; Afolabi, A.E.; Anamu, U.S.; Olorundaisi, E.; Umba, M.C.; Phahlane, T.; Ayodele, O.O.; Olubambi, P.A. Exploring high entropy alloys: A review on thermodynamic design and computational modeling strategies for advanced materials applications. *Heliyon* **2024**, *10*, e39660. [CrossRef]
2. George, E.P.; Raabe, D.; Ritchie, R.O. High-entropy alloys. *Nat. Rev. Mater.* **2019**, *4*, 515–534. [CrossRef]
3. Mitra, R.; Bajpai, A.; Biswas, K. A critical review on mechanical alloying of high-entropy materials. *High Entropy Alloys Mater.* **2025**, *3*, 1–40. [CrossRef]
4. Yeh, J.-W.; Chen, S.K.; Lin, S.-J.; Gan, J.-Y.; Chin, T.-S.; Shun, T.-T.; Tsau, C.-H.; Chang, S.-Y. Nanostructured high-entropy alloys with multiple principal elements: Novel alloy design concepts and outcomes. *Adv. Eng. Mater.* **2004**, *6*, 299–303. [CrossRef]
5. Cantor, B.; Chang, I.T.H.; Knight, P.; Vincent, A.J.B. Microstructural development in equiatomic multicomponent alloys. *Mater. Sci. Eng. A* **2004**, *375–377*, 213–218. [CrossRef]
6. Hamdi, H.; Abedi, H.R.; Zhang, Y. A study on outstanding high-temperature wear resistance of high-entropy alloys. *Adv. Eng. Mater.* **2023**, *25*, 2201915. [CrossRef]
7. Gopinath, V.M.; Arulvel, S. A review on the steels, alloys/high entropy alloys, composites and coatings used in high temperature wear applications. *Mater. Today Proc.* **2021**, *43*, 817–823. [CrossRef]
8. Han, Y.; Fu, H. Improvement of high temperature wear resistance of laser-cladding high-entropy alloy coatings: A review. *Metals* **2024**, *14*, 1065. [CrossRef]
9. Zhang, Y.; Zhang, B.; Li, K.; Zhao, G.-L.; Guo, S.M. Electromagnetic interference shielding effectiveness of high entropy AlCoCrFeNi alloy powder laden composites. *J. Alloys Compd.* **2018**, *734*, 220–228. [CrossRef]
10. Wang, R.; Zhang, K.; Davies, C.; Wu, X. Evolution of microstructure, mechanical and corrosion properties of AlCoCrFeNi high-entropy alloy prepared by direct laser fabrication. *J. Alloys Compd.* **2017**, *694*, 971–981. [CrossRef]
11. Kratochvíl, P.; Průša, F.; Thürlová, H.; Strakošová, A.; Karlík, M.; Čech, J.; Haušild, P.; Čapek, J.; Ekrt, O.; Jarošová, M.; et al. The role of the preparation route on microstructure and mechanical properties of AlCoCrFeNi high entropy alloy. *J. Mater. Res. Technol.* **2024**, *30*, 4248–4260. [CrossRef]
12. Faraji, A.; Farvizi, M.; Ebadzadeh, T.; Kim, H.S. Microstructure, wear performance, and mechanical properties of spark plasma-sintered AlCoCrFeNi high-entropy alloy after heat treatment. *Intermetallics* **2022**, *149*, 107656. [CrossRef]
13. Li, S.; Ding, J.; Liu, Z.; Wang, X.; He, P.; Narayanan, J.A.; Du, S.; Zhou, L. Evolution of microstructure and properties of AlCoCrFeNi high-entropy alloy coatings fabricated at different laser power levels. *Mater. Today Commun.* **2025**, *46*, 112644. [CrossRef]
14. Cheng, J.; Xing, Y.; Dong, E.; Zhao, L.; Liu, H.; Chang, T.; Chen, M.; Wang, J.; Lu, J.; Wan, J. An overview of laser metal deposition for cladding: Defect formation mechanisms, defect suppression methods and performance improvements of laser-cladded layers. *Materials* **2022**, *15*, 5522. [CrossRef]
15. Yan, L.; Chen, Y.; Liou, F. Additive manufacturing of functionally graded metallic materials using laser metal deposition. *Addit. Manuf.* **2020**, *31*, 100901. [CrossRef]
16. Hedayatnejad, R.; Sabet, H.; Rahmati, S.; Golezani, A.S. Investigation of additive manufacturing process by LMD method, affecting process parameters on microstructure and quality of deposition layers. *J. Environ. Friendly Mater.* **2021**, *5*, 47–58.
17. Gu, D.D.; Meiners, W.; Wissenbach, K.; Poprawe, R. Laser additive manufacturing of metallic components: Materials, processes and mechanisms. *Int. Mater. Rev.* **2012**, *57*, 133–164. [CrossRef]
18. Selcuk, C. Laser metal deposition for powder metallurgy parts. *Powder Metall.* **2011**, *54*, 94–99. [CrossRef]

19. Dobrzanski, L.; Jonda, E.; Lukaszkowicz, K.; Labisz, K.; Klimpel, A. Surface modification of the X40CrMoV5-1 steel by laser alloying and PVD coatings deposition. *J. Achiev. Mater. Manuf. Eng.* **2008**, *27*, 179–182.
20. Li, X.; Zhang, C.; Zhang, S.; Wu, C.; Zhang, J.; Chen, H.; Abdullah, A.O. Design, preparation, microstructure and properties of novel wear-resistant stainless steel-base composites using laser melting deposition. *Vacuum* **2019**, *165*, 139–147. [CrossRef]
21. Liu, W.; Song, J.; Li, W.; Ma, Z.; Liu, H.; Liu, B.; Zhao, Y.; Wang, F. Research progress on structure and performance of metal (steel and titanium) matrix composite materials manufactured by laser additive manufacturing: A review. *Int. J. Adv. Manuf. Technol.* **2025**, *140*, 4643–4678. [CrossRef]
22. Shi, Y.; Gong, S.; Xu, H.; Chen, W.; Wang, Z.; Yang, G.; Qi, B. In-situ multi-principal element alloying of equiaxed and lamellar tial alloys via electron beam freeform fabrication with dual-wire synergistic control. *SSRN Sch. Pap.* **2024**, 4830412. [CrossRef]
23. Xiao, X.; Lu, C.; Fu, Y.; Ye, X.; Song, L. Progress on experimental study of melt pool flow dynamics in laser material processing. In *Liquid Metals*; IntechOpen: London, UK, 2021. [CrossRef]
24. Gan, Z.; Yu, G.; He, X.; Li, S. Numerical simulation of thermal behavior and multicomponent mass transfer in direct laser deposition of Co-base alloy on steel. *Int. J. Heat Mass Transf.* **2017**, *104*, 28–38. [CrossRef]
25. Shi, B.; Attia, H. Current status and future direction in the numerical modeling and simulation of machining processes: A critical literature review. *Mach. Sci. Technol.* **2010**, *14*, 149–188. [CrossRef]
26. Norton, T.; Tiwari, B.; Sun, D.-W. Computational fluid dynamics in the design and analysis of thermal processes: A review of recent advances. *Crit. Rev. Food Sci. Nutr.* **2013**, *53*, 251–275. [CrossRef]
27. Trzepieciński, T.; Dell'Isola, F.; Lemu, H.G. Multiphysics modeling and numerical simulation in computer-aided manufacturing processes. *Metals* **2021**, *11*, 175. [CrossRef]
28. Picasso, M.; Hoadley, A.F.A. Finite element simulation of laser surface treatments including convection in the melt pool. *Int. J. Numer. Methods Heat Fluid Flow* **1994**, *4*, 61–83. [CrossRef]
29. Qi, H.; Mazumder, J.; Ki, H. Numerical simulation of heat transfer and fluid flow in coaxial laser cladding process for direct metal deposition. *J. Appl. Phys.* **2006**, *100*, 24903. [CrossRef]
30. Ma, C.; Zhang, R.; Li, Z.; Jiang, X.; Wang, Y.; Zhang, C.; Yin, H.; Qu, X. An integrated multiscale model to study the marangoni effect on molten pool and microstructure evolution. *Integr. Mater. Manuf. Innov.* **2023**, *12*, 502–513. [CrossRef]
31. Li, Z.; Yu, G.; He, X.; Li, S.; Shu, Z. Surface tension-driven flow and its correlation with mass transfer during L-DED of Co-based powders. *Metals* **2022**, *12*, 842. [CrossRef]
32. Körner, C.; Markl, M.; Koepf, J.A. Modeling and simulation of microstructure evolution for additive manufacturing of metals: A critical review. *Metall. Mater. Trans. A* **2020**, *51*, 4970–4983. [CrossRef]
33. Ma, L.; Liu, H.; Williams, M.; Levine, L.; Ramazani, A. Integrating phase field modeling and machine learning to develop process-microstructure relationships in laser powder bed fusion of IN718. *Metall. Microstruct. Anal.* **2024**, *13*, 983–995. [CrossRef]
34. Chen, B.; Zhao, Y.; Yang, H.; Zhao, J. Process parameters optimization and numerical simulation of AlCoCrFeNi high-entropy alloy coating via laser cladding. *Materials* **2024**, *17*, 4243. [CrossRef] [PubMed]
35. Tian, H.; Chen, X.; Yan, Z.; Zhi, X.; Yang, Q.; Yuan, Z. Finite-element simulation of melt pool geometry and dilution ratio during laser cladding. *Appl. Phys. A* **2019**, *125*, 485. [CrossRef]
36. Moldovan, E.R.; Doria, C.C.; Ocaña, J.L.; Istrate, B.; Cimpoesu, N.; Baltes, L.S.; Stanciu, E.M.; Croitoru, C.; Pascu, A.; Munteanu, C.; et al. Morphological analysis of laser surface texturing effect on AISI 430 stainless steel. *Materials* **2022**, *15*, 4580. [CrossRef] [PubMed]
37. Jie, D.; Wu, M.; He, R.; Cui, C.; Miao, X. A multiphase modeling for investigating temperature history, flow field and solidification microstructure evolution of FeCoNiCrTi coating by laser cladding. *Opt. Laser Technol.* **2024**, *169*, 110197. [CrossRef]
38. Okunkova, A.; Volosova, M.; Peretyagin, P.; Vladimirov, Y.; Zhirnov, I.; Gusarov, A. Experimental approbation of selective laser melting of powders by the use of non-gaussian power density distributions. *Phys. Procedia* **2014**, *56*, 48–57. [CrossRef]
39. Murzin, S.P.; Bielak, R.; Liedl, G. Algorithm for calculation of the power density distribution of the laser beam to create a desired thermal effect on technological objects. *Comput. Opt.* **2016**, *40*, 679–684. [CrossRef]
40. Wang, S. Extensions to the navier–stokes equations. *Phys. Fluids* **2022**, *34*, 53106. [CrossRef]
41. Ikeshoji, T.; Hafskjold, B. Non-equilibrium molecular dynamics calculation of heat conduction in liquid and through liquid-gas interface. *Mol. Phys.* **1994**, *81*, 251–261. [CrossRef]
42. Kumar, V.; Durst, F.; Ray, S. Modeling moving-boundary problems of solidification and melting adopting an arbitrary lagrangian-eulerian approach. *Numer. Heat Transf. Part B* **2006**, *49*, 299–331. [CrossRef]
43. Otto, T.; Rossi, M.; Boeck, T. Viscous instability of a sheared liquid-gas interface: Dependence on fluid properties and basic velocity profile. *Phys. Fluids* **2013**, *25*, 32103. [CrossRef]
44. Chakraborty, N. Thermal transport regimes and effects of prandtl number in molten pool transport in laser surface melting processes. *Numer. Heat Transf. Part A* **2007**, *53*, 273–294. [CrossRef]

45. Nogi, K.; Ogino, K.; McLean, A.; Miller, W.A. The temperature coefficient of the surface tension of pure liquid metals. *Metall. Trans. B* **1986**, *17*, 163–170. [CrossRef]
46. Mayer, S.W. A molecular parameter relationship between surface tension and liquid compressibility. *J. Phys. Chem.* **1963**, *67*, 2160–2164. [CrossRef]

Disclaimer/Publisher's Note: The statements, opinions and data contained in all publications are solely those of the individual author(s) and contributor(s) and not of MDPI and/or the editor(s). MDPI and/or the editor(s) disclaim responsibility for any injury to people or property resulting from any ideas, methods, instructions or products referred to in the content.